Journal of Nepal Geological Society, 2023, Vol. 66, pp. 37–52
https://doi.org/10.3126/jngs.v66i01.57921

Failure mechanism of large-scale landslide in the central Nepal Himalaya

Bikash Phuyal[1] and Prem Bahadur Thapa[2,*]

[1]Central Department of Geology, Tribhuvan University, Kirtipur, Kathmandu, Nepal
[2]Department of Geology, Tri-Chandra Multiple Campus, Tribhuvan University, Kathmandu, Nepal
**Corresponding author's email: prem.thapa@trc.tu.edu.np*

ABSTRACT

The geomorphological and geological characteristics of central Nepal reflect the dynamic nature of tectonic and mass movement processes that lead to the occurrence of large-scale landslides (LSLs). The mechanism of the LSL failure process is not well understood due to the different deformation stages controlled by geological structures and causative/triggering factors. Regional tectonic structures and local rock mass characteristics play a vital role in the formation of LSLs. Engineering geological characterization was performed to evaluate the rock/soil properties, and the associated state of danger (cracks, seepage, etc.). The rock mass rating (RMR) and geological strength index (GSI) methods were used to estimate rock mass quality and strength parameters. The estimated strength parameters together with laboratory test data were used to set up a two-dimensional (2D) landslide surface to simulate the failure scenarios. The simulation of landslide models was iterated under different loading conditions by incorporating geological heterogeneities. The results have demonstrated that the movement of the slope was affected by different stress conditions over time, which were verified using spatiotemporal landslide data. The landslide exhibited a three-stage failure mechanism with the development of tension-induced cracking at the rear and shearing failure of the critical locking section in the middle section. The tension shear and joint-step-path rupture along joint surfaces occurred during different stages of the landslide failure processes. The simulated results showed that the genetic development of LSL is mainly attributed to the geological structures and sudden changes in stress conditions. Thus, the research outcomes can be illustrative to evaluate the role of geological discontinuities, geotechnical parameters and triggering effects by the numerical simulation techniques for the failure mechanism of LSLs.

Keywords: Large-scale landslide, failure mechanism, modelling, central Nepal

Received: 25 March 2023 **Accepted:** 27 May 2023

INTRODUCTION

The slope dynamics of the Himalaya are complex due to the interplay of tectonic forces, climatic processes, and geological factors. Landslides in the Himalayan region are a frequent occurrence varying in scale and used to classify based on factors such as the materials involved, area/volume of the landslide, type of movement, origin in terms of geological and structural controls (Varnes, 1978; Cruden and Varnes, 1996; Huang 1996a,b; Wang and Zhang, 1983; Brueckl and Parotidis, 2001; Wen and Chen, 2007; Lin et al., 2013; Hungr et al., 2014; Zerathe et al., 2014; Zhou and Cheng, 2015; Chung et al., 2018; Kuo et al., 2018; Cui et al., 2022). The rainfall parameters; duration and accumulated rainfall are more pronounced on LSLs compared to smaller landslides (Kuo et al., 2018). Similarly, distance, direction, seismic locked zone, geometry of fault/thrust can affect the spatial occurrences of large-scale landslides (Xu et al., 2011). The unique geological and tectonic characteristics of the central Nepal Himalaya along with the influence of monsoonal rainfall contribute to the occurrence of a number of slope failures (Nepal et al., 2019; Phuyal et al., 2022).

The mechanism of LSLs are addressed by some researchers to understand the occurrence of the LSLs in complex geo-tectonic settings (Wilson et al., 2003; Zerathe et al., 2014; Ghobadi et al., 2017). The geological characteristics of an area particularly the orientation of rock strata in relation to the slope play a significant role in LSL formation (Chung et al., 2017; Ghobadi et al., 2017). The presence of inter-bedded rock strata with different mechanical properties is another important geological factor (Zerathe et al., 2014; Zhao et al., 2019). The distribution pattern of LSL indicated a strong correlation with seismic faults or thrusts (Huang and Li, 2008, 2009), with many LSLs aligning perpendicular to the regional thrust system and being located in close proximity to the fault or thrust (Timilsina et al., 2012; Zhao et al., 2019). Some studies have shown that the geo-morphometric characteristics also strongly influence the distribution of LSL in the Nepal Himalaya (Hasegawa et al., 2008; Timilsina et al., 2012).

The failure characteristics of landslides in central Nepal have been studied by various researchers focusing on the role of causative and triggering factors (Caine and Mool, 1982; Gerrard, 1994; Dahal et al., 2006; Dahal and Hasegawa, 2008; Thapa, 2011; Regmi et al., 2012; Devkota et al., 2013; Pathak, 2016; Gadtaula and Dhakal, 2019; Phuyal et al., 2022). However, limited research has been conducted on the failure process and mechanism of large-scale landslides (LSLs). In this conceptual framework, the present research has modelled the LSL numerically to illustrate the failure mechanism in central Nepal Himalaya.

SETTING OF THE AREA

The central Nepal exhibits diverse geomorphological and geological characteristics. The area is dominated by mountains and hills ranging from an elevation of 170 to 4595 m (Fig. 1a). Central Nepal is characterized by numerous river valleys that cut through the rugged terrain and the occurrence of a number of landslides including LSLs is common due to the prevalence of geo-environmental settings (Fig. 1b,c). Among the LSLs, the Jure Landslide (27.77077° N, 85.867868° E) of Sindhupalchowk District is considered in this study (Fig. 1b). The geological and structural characteristics of central Nepal Himalaya are complex and are divided into various tectonic divisions, namely Sub-Himalaya, Lesser Himalaya, Higher Himalaya, and Tethys Himalaya. The rock sequences in the central Nepal Himalaya have been described chronologically and different thrusts separate these rock formations (Fig. 2). The tectonic structures, such as the Midland Antiform, Great Mahabharat Synclinorium, Okhaladhunga Window, and Kathmandu Nappe, have undergone significant deformation within the rock strata of the region (Stöcklin and Bhattarai, 1977; Dhital, 2015). The intense deformation caused by these structures could potentially serve as a significant factor in initiating and propagating large-scale landslides in the area (Dhital, 2015).

ENGINEERING GEOLOGICAL CHARACTERIZATION

The lithological and structural features were extracted from the existing geological maps (DMG, 1980; Dhital, 2015) and updated by field investigations. The fieldwork in modelling site

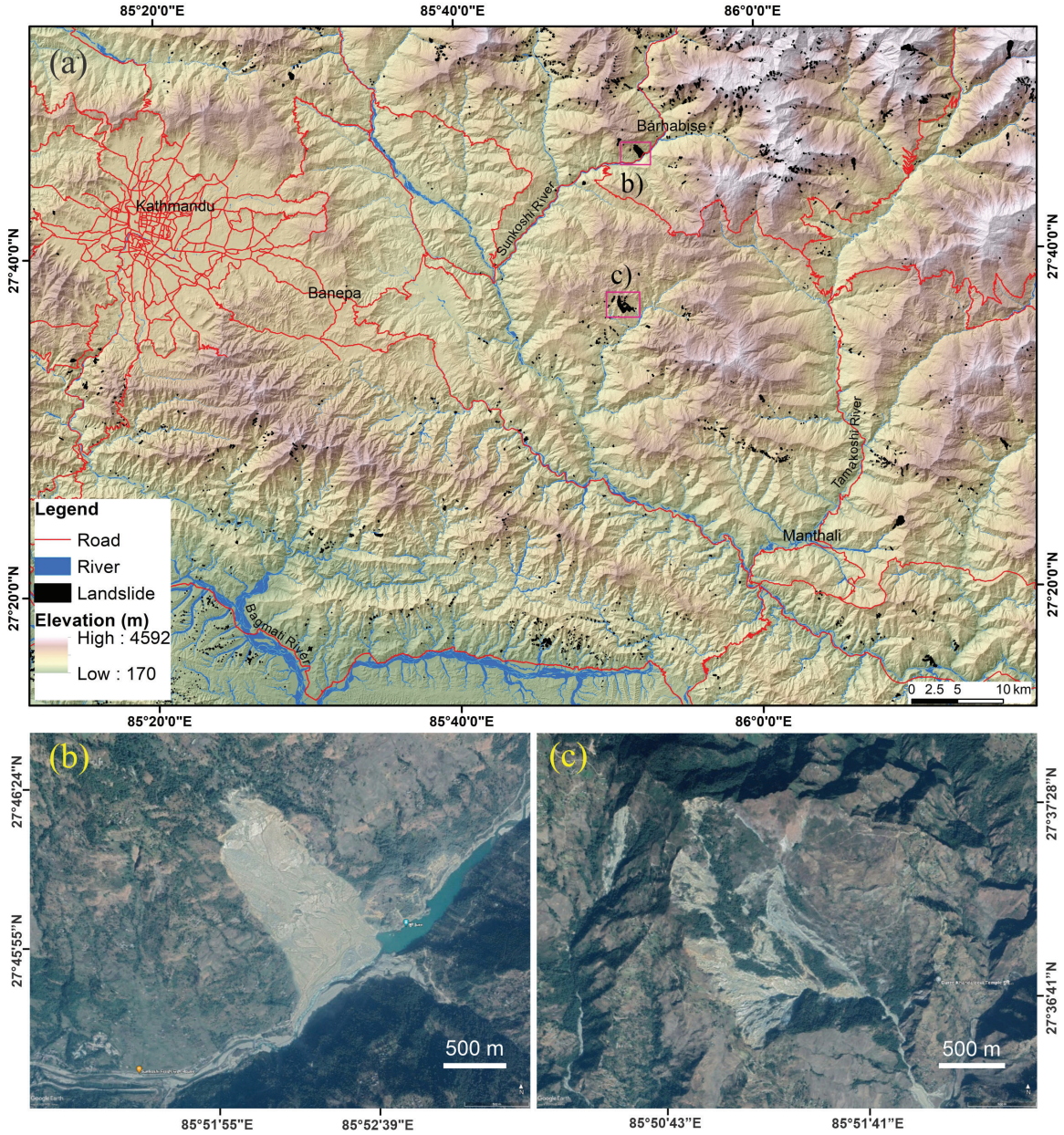

Fig. 1: Study area showing the distribution of landslides (a) elevation map, (b) Jure Landslide occurred at Sindhupalchok on 2nd August 2014, (c) Dutti Landslide at Chaurideurali, Kavre.

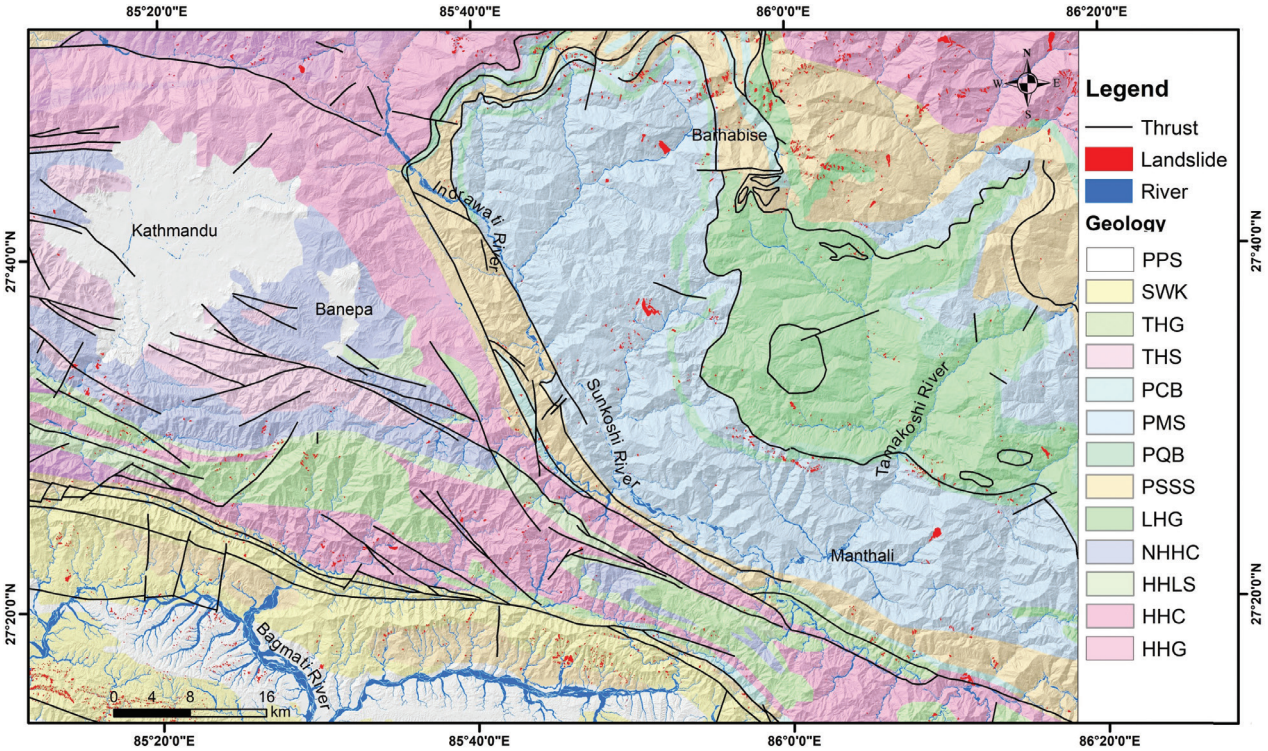

Fig. 2: Regional Geological map of the area (DMG, 1980; Dhital, 2015). Higher Himalayan Sequence; HHG – Gneiss, HHC- crystalline sequence (Ppx), HHLS – lime silicate (Ppx), NHHS - crystalline (Ppz). Lesser Himalayan Sequence; LHG – gneiss (Ppx), PSSS –slate, siltstone, sandstone, shale (Prz), PQB – quartzite band (Prz), PMS – phyllite, metasandstone, schist (Prz), PCB – carbonate bands (Prz). Tethys Himalayan Sequence; THS – Tethys Himalayan Sequence (Pz), THG – gneiss (Pz). SWK – Siwaliks (N), PPS – Plio-Pleistocene sediments. Ppx = Paleo-proterozoic, Ppz = Neo-proterozoic, Prz = Proterozoic, Pz = Paleozoic, N = Neogene.

and adjoining area was focused on detailing the engineering geological characteristics of large-scale landslides that can have an inherent role from the perspectives of geomorphological and structural geological control on the mechanism of landslide failure processes. The characterization process involved the interpretation of satellite images which provided morphometry of the model landslide. On-site measurements were carried out to collect data on geological structures such as the geometry of strata, faults, rock discontinuities, etc. A collected dataset of the discontinuity sets was compiled and analysed based on rock mass properties. Oriented data were represented in stereo-plots to examine the probability of failure modes (plane, wedge, toppling). The methodological approach used is shown in Figure 3.

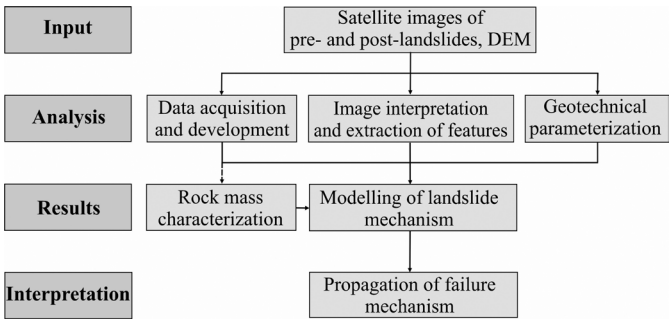

Fig. 3: Workflow of methodology adopted in the study.

Discontinuity properties and kinematic analysis

The source area of the landslide possesses distinctive topographic features resembling a chair shape which is revealed from satellite images and field observation. The steeply dipping joint and foliation surface form the left flank of the slide in the northern part whereas two prominent joint sets constitute the right flank (Fig. 4a). The primary body of the landslide consists of a deformed rock mass that underwent tension failure due to pore water pressure within the sliding mass.

A fracture along a joint surface with a maximum height of 50 m is observed on the northern flank of the source area, following a direction of J_1: 86°/179°. This scarp exhibits major two sets of joints with an orientation range of 264–298° having a dip range of 50–70° and another with an orientation range of 335–352° associated with a dip range of 23–50°. A highly persistent shear joint is found distinctly parallel to the stress release joint (J_1) along the slope with steeper than slope face. The detached rock boulders having a range of up to 20 m are lying over the upper benching slope of landslides (Fig 4b,c).

The southern flank surface, dipping towards the northeast is characterized by a steep inclined joint planar surface with an orientation of 82°/065°. Groundwater consistently flowing from the weak planer surface of the steep head scarp (Fig. 4d). The weak zone passes from the southern flank to northern flank across the head scarp that has distinguished the boundary of highly weathered rocks and brittle high metamorphic rock strata (Fig. 4e). This planer surface is parallel to the foliation that follows a mean orientation of 352° with a dip of 23° (Fig.

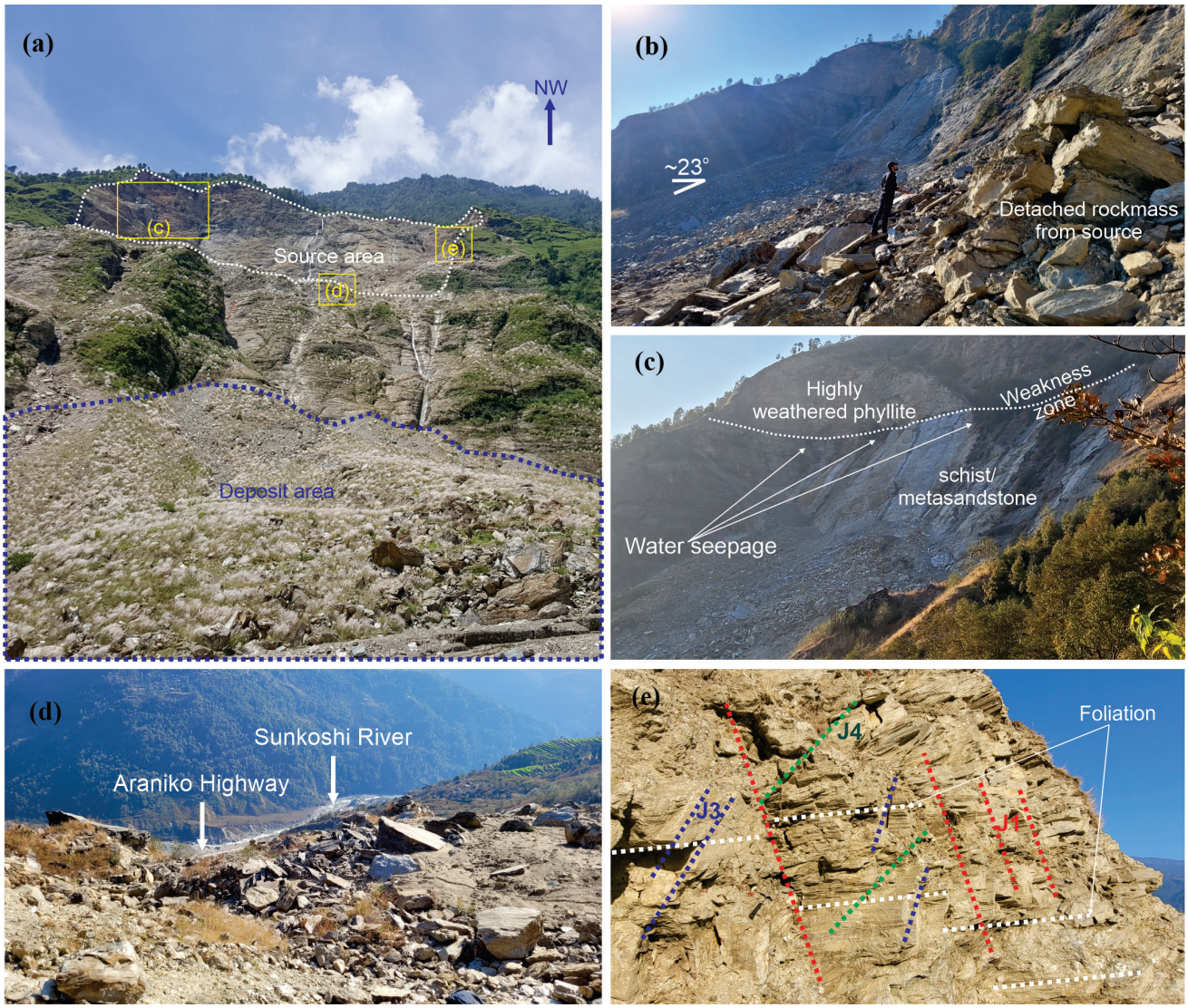

Fig. 4: Field photographs of landslide components (a) main body of landslide, (b) head scarp, (c) landslide rock debris, (d) inter-stratum boundary and seepage condition, (e) sets of discontinuities present in the landslide flank.

5). The distribution density of discontinuities was graphically represented (Fig. 5a,b,c). The kinematic analysis of probable failure modes based on the slope geometry and orientation of discontinuities are shown in Figures 5d,e,f.

Rock mass classification

The geological strength index (GSI) developed by Hoek and Brown (1997) was implemented to obtain a precise assessment of the quality of the rock mass (Hoek, 1994; Hoek et al., 1995). The GSI is based on the quantitative evaluation of the rock mass structure by considering factors such as block geometry, presence of discontinuities, and surface conditions including roughness, joint infill, and weathering. The surface condition rating (SCR) and structure rating (SR) were additionally incorporated for the accuracy of GSI values. These two additional parameters help to get the characteristics of the blockiness and surface conditions of the rock structures. The SCR is derived using Equation 1.

$$SCR = R_r + R_w + R_f \quad (1)$$

where, R_r, R_w, and R_f are the roughness rating, weathering rating, and infill rating respectively. The SCR axis is divided into 18 equal divisions (Sonmez and Ulusay, 1999), and the maximum sum of roughness, weathering, and infill rating was calculated as a value of 18 in exposed rock mass in the landslide area. The SR designated the structure of the rock mass based on the volumetric joint count (J_v) which is estimated by using the relation (Eq. 2).

$$J_v = \frac{N_1}{L_1} + \frac{N_2}{L_2} + \cdots + \frac{N_n}{L_n} \quad (2)$$

where, N, L and n are the parameters as number of joints along the scanline, length of scanline, and number of joint sets used to calculate J_v.

Sonmez and Ulusay (1999) established a graphical relation by comparing the J_v values of each category with the boundary values of the SR (Fig. 4). This graphical plot is based on the volumetric joint counts and calculated the SR rating of the rock mass. The GSI values were estimated from the calculated values of SCR and SR ratings. The GSI value assigned to each

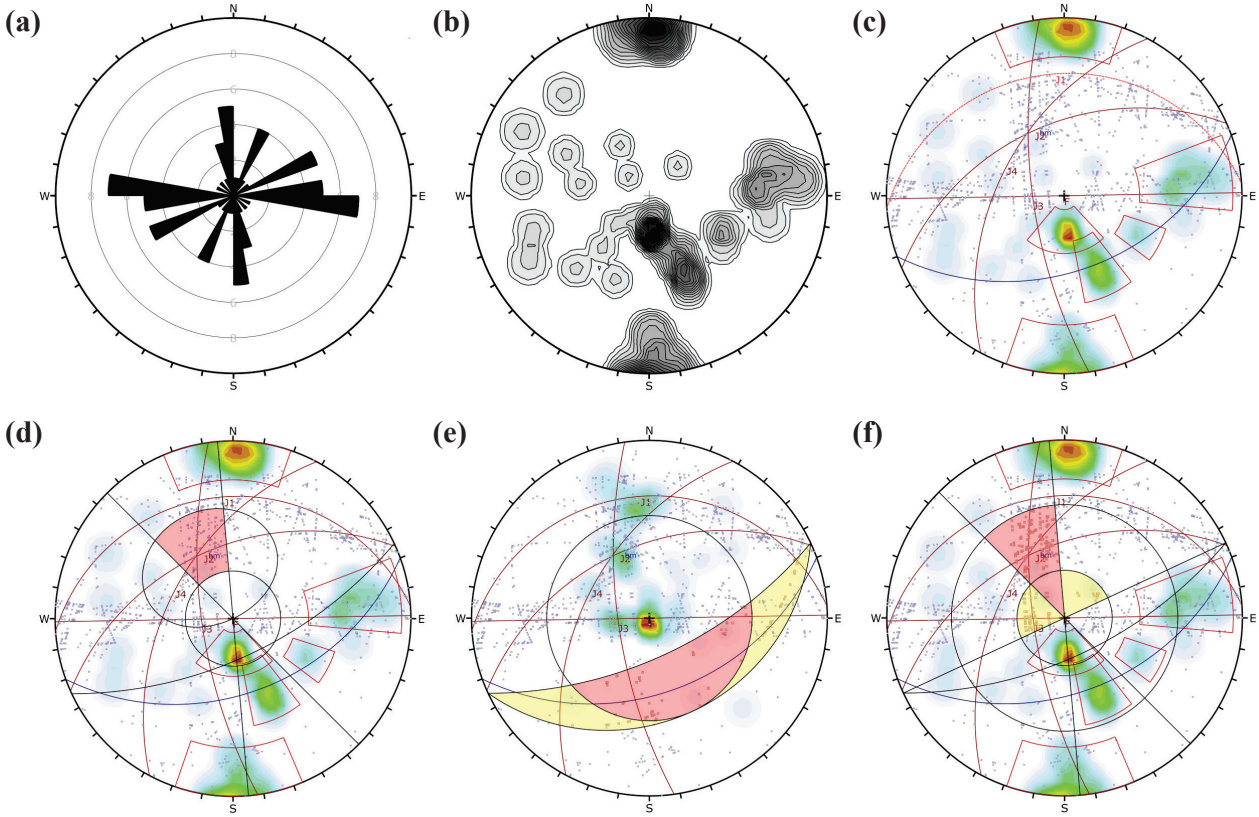

Fig. 5: Discontinuities characteristics representation (a) rose plot of discontinuities, (b) contour plot of pole concentration, (c) major mean joint sets and potential failure modes (d) plane failure, (e) wedge failure, (f) toppling failure with respect to the slope geometry.

rock mass in the site represented an average value ranging from 50 to 100 m^2. Marinos et al. (2005) suggested estimating GSI value in increments of 10 (e.g., 0–10, 10–20, and 20–30) to assess the quality of the rock mass. The rock mass rating (RMR) system proposed by Bieniawski (1979, 1989) has been also used to calculate geological and geotechnical parameters for a quantitative assessment of the rock mass quality and its influence on slope stability. Moreover, the rock quality designation (RQD) was determined using Equation 3 (Palmstrom, 2005) and Equation 4 (Bieniawski, 1979, 1989). The assigned GSI value for each rock mass was validated with the calculated GSI from the relationship of Equations 5 (Bieniawski, 1989).

$$RQD = 115 - 3.3\,J_v \tag{3}$$

$$RMR = R_{UCS} + R_{RQD} + R_{JS} + R_{JC} + R_{GW} \tag{4}$$

$$GSI = RMR - 5 \text{ for } RMR > 23 \tag{5}$$

where, R_{UCS}, R_{RQD}, R_{JS}, R_{JC}, *and* R_{GW} are the ratings for the strength, RQD, JS, JC, and GW condition of the rock mass.

The properties of rock discontinuities are given in Table 1 which is a prerequisite for GSI estimation. The GSI of the rock mass on the sliding surface is ranged from 30 to 45, while the GSI of the rock mass on the main scarp is in the range of 40–65 (Fig. 6). The estimated GSI values from on either side of landslide is similar which fall within 25–40 and a lower value is attributed to poor rock mass quality.

Geological and structural controls

Some research works carried out in the past decade based on the generic evolution of large-scale landslides are closely related to the unique characteristics of rock structures as well as the processes of deformation and failure (Huang, 2011). It has been observed that these landslides were primarily triggered by an abrupt brittle failure of the locking section along the potential sliding surface (Huang, 1996a,b; Huang, 2011). Failure mechanisms of large-scale landslide described by those researchers are based on the three-section (creep-tension-shear) failure that encompasses three stages of deformation and failure; gradual movement along inclined structural planes, tension-induced cracking at the rear and shearing failure of the critical locking section in the middle (Zhang et al., 1990; Huang, 1996a). The presence of this resilient component acting as a barrier to obstruct slope deformation plays a vital role in maintaining slope stability. As creeping and cracking progress, stress gradually accumulates on the resistant section (Fig. 7a). Such kind of failure mechanism is typically observed in slopes composed of brittle rocks with horizontal to gently incline structural planes near the base of the slope consisting of interlayered hard and soft rocks. Examples of this deformation and failure mechanism are mentioned by Zhang et al. (1990) to illustrate the large-scale and high-speed landslide in the vicinity of Longxia Hydropower Station on the Yellow River. Similar mechanisms have also been identified in the failures at the Laxiwa Hydropower Station on the Yellow River and the Yanchi phosphor mine in Hubei (Huang and Deng, 1993; Huang, 1996a,b).

An alternative form of failure mechanism is known as the retaining wall collapse mechanism, which is distinguished by

Table 1: Major discontinuity sets (average orientation extracted from Dips) and their properties extracted from direct field observation and measurement.

Discontinuity	Mean dip		Persistence	Spacing	Roughness	Opening	Weathering
	Amount	Direction					
F	23	352	3–10 m	200–600 mm	R/S	1–5 mm	SW/MW
J_1	86	179	1–3 m	60–200 mm	SR/S	>5 mm	SW/MW
J_2	50	335	1–3 m	60–200 mm	SR/S	1–5 mm	SW/MW
J_3	70	264	1–3 m	60–200 mm	SR/S	>5 mm	SW/HW
J_4	50	298	<1 m	60–200 mm	R/S	>5 mm	SW/HW

Note: SW-slightly weathered, MW-moderately weathered, HW-highly weathered, R - rough, S-smooth, SR-slightly rough, F - foliation, J - joint.

Fig 6: Rock mass quality and the corresponding GSI estimates from different location of landslide (i) main scarp, (ii) sliding surface, (iii) landslide flanks.

a loose structure throughout the slope, except for relatively rigid geological formations located in the middle or front portions. These rigid sections possess exceptionally high strength, functioning as a retaining wall (Huang, 1996a,b). The rigid segment typically experiences significant pressure due to the deformation of the overlying sliding mass. Similar to the locking section, the rigid part plays a pivotal role in upholding slope stability (Huang et al., 1991; Huang et al., 2002a,b). As deformation progresses the rigid section undergoes sudden brittle shear failure potentially leading to the rapid development of a landslide. Notable examples of retaining wall collapse landslides include the Xikou landslide in Sichuan and the Touzhai landslide in Zhaotong, Yunnan. The fundamental characteristics of this slope failure mechanism is illustrated in Figure 7b (Huang, 1996a,b).

Translational landslides can evolve into a large-scale slide that typically develops in nearly horizontal bedrock formations (Fig. 7c). These landslides are primarily triggered by a combination of hydrostatic and uplift pressures (Zhang et al., 1994; Wang and Zhang, 1983). It is believed that large-scale landslides are improbable in slopes with counter-inclined rock strata. The general opinion proposes that toppling deformation is limited to the uppermost tens of meters in counter-dip strata which is illustrated in Figure 7d,e for visual support to the notion. However, in the past two decades, southwest China has witnessed deep bending and toppling deformations reaching depths of 200–300 m, leading to the occurrence of extensive, deep-seated landslides (Zhang et al., 1994; Wang, 1992).

A number of research studies have been conducted over the past four decades to investigate the failure mechanism of lamellar rock slopes (Zhang et al., 1994; Lo et al., 1978; Broadbent and Ko, 1971). These researches have revealed the lamellar rock slopes can be categorized into two types based on the dip angle of the sliding plane. In the first category, the dip angle of the sliding plane is less than the slope angle making the potential sliding plane visible on the slope or in excavations (Gerrad, 1994; Petley, 2007). In such cases, the deformation mechanism is relatively straightforward and can

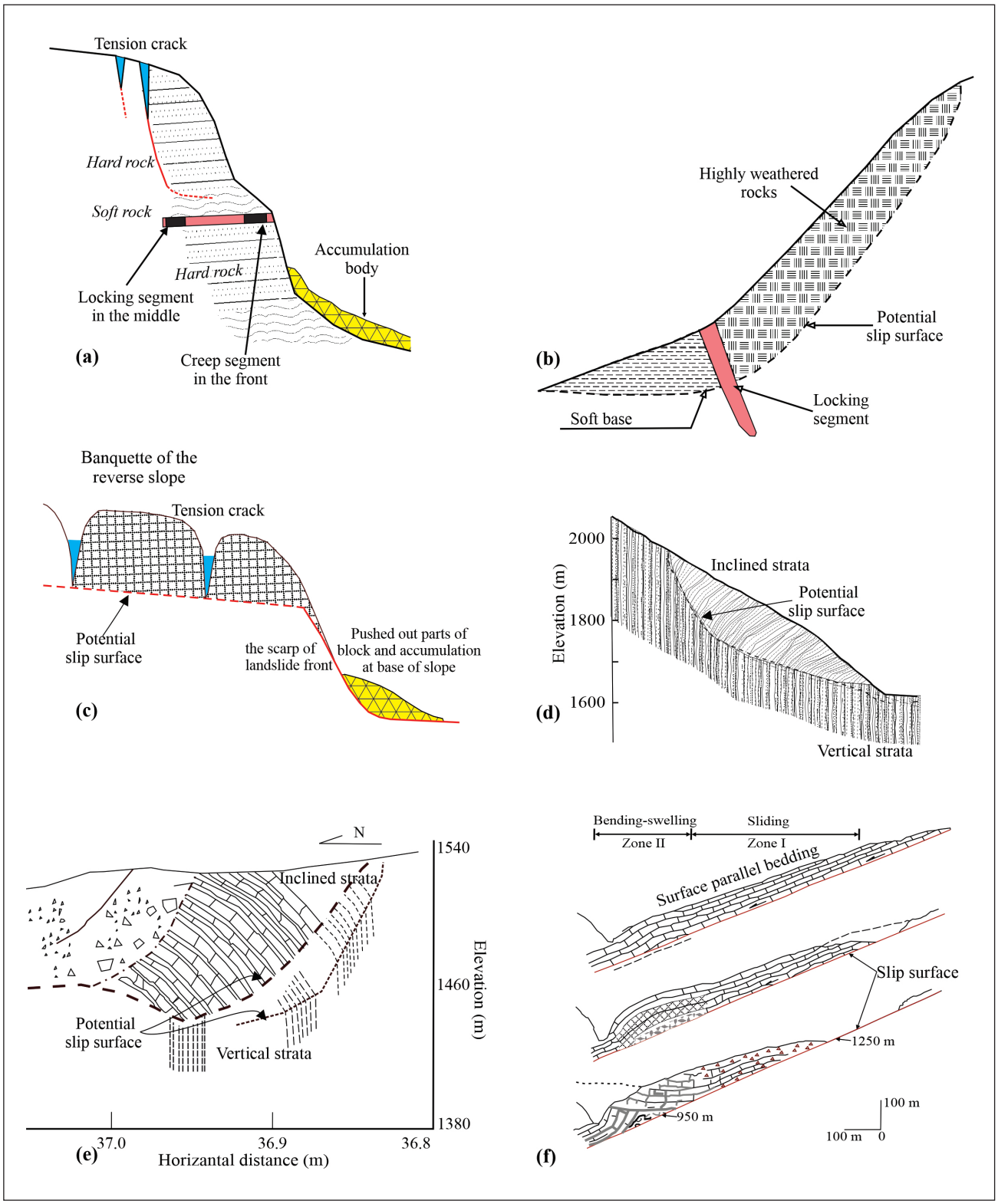

Fig. 7: Conceptual models (redrawn from Huang, 2011) (a) three-section (creep-tension-shearing) mechanism (Zhang et al., 1990; Huang, 1993), (b) retailing wall collapse mechanism (Huang, 1996a,b), (c) translation mechanism (Huang 2011), (d) toppling deformation process (Wang et al., 1995), (e) toppling deformation structure, (f) deformation and failure of cataclinal rock slopes (Zhang et al., 1994).

be described as a creep-sliding and cracking or movement along the potential sliding plane. The position of the sliding plane and corresponding stability conditions can be easily identified. The formation process of slopes in this category is relatively short, leading to sudden failure (Lo et al., 1978; Broadbent and Ko, 1971; Huang, 2011). It is crucial to identify the position of the potential sliding plane and monitor slope deformation during construction for this type of slope (Fig. 7f). The second category involves potential sliding planes that dip more steeply than the slope surface. Large-scale landslides often fall into this category, posing a greater risk compared to the first category. The formation of the sliding plane in this case is a complex geological and mechanical process, making it challenging to identify (Zhang et al., 1994; Lo et al., 1978; Broadbent and Ko, 1971; Huang et al., 2002a; Huang, 2011). The large-scale failure mechanism is also conceptualized by cataclinal lamellar rock slopes as sliding-bending-shearing or sliding-shearing, which is closely linked to the presence of weak layers within the rock strata (Zhang et al., 1994; Huang et al., 2002a). Based on different deformation characteristics, the slope can be divided into a sliding part in the upper head and middle of the slope and a bending-swelling part in the lower section. When bending-swelling deformations progressed, the resistant part of the slope underwent shearing resulting in landsliding events (Fig. 7f).

NUMERICAL MODELLING

Numerical modeling serves as a valuable supplementary tool to complement experimental activities based on physical models. In fact, the progressive utilization of numerical modelling techniques has contributed to the advancement of our understanding of the intricate physical phenomena underlying the processes of landslide generation and propagation (Crosta et al., 2003; Romano, 2020). Specifically, the application of large deformation numerical simulations has proven to be an effective means of capturing the movement characteristics exhibited by landslides. This approach yields pertinent insights into the initiation and runout behaviours of landslides which hold significant importance in the context of hazard assessment, particularly in mountainous regions (Lei et al., 2022; Nguyen et al., 2022).

Conceptual approach and model setup

The fundamental conceptual approach was followed which requires the parameters that include the uniaxial compressive strength (UCS), tensile strength (TS), Young's modulus (E), cohesion strength (c), and angle of internal friction (ϕ) were determined from laboratory tests. Known values were also taken into consideration from the literature as input parameters. In modelling process, the generalized Hoek-Brown failure criterion for jointed rock masses was used to quantify the rock mass stability condition in the landslide area (Eq. 6).

$$\sigma_1' = \sigma_3' + \sigma_{ci}\left(m_b \frac{\sigma_3'}{\sigma_{ci}} + s\right)^a \quad (6)$$

where, σ_1' and σ_3' are the maximum and minimum effective principal stresses at failure, m_b represents the Hoek-Brown constant for the rock mass, while s and a are constants that rely on the specific characteristics of the rock mass. Additionally, σ_{ci} denotes the uniaxial compressive strength of the individual intact rock pieces.

A numerical value derived from GSI was considered together with intact rock properties to estimate the reduced rock mass strength under various geological conditions (Equations 7,8,9). The adjustment factor *'D'* of Hoek-Brown failure criterion for rock strata disturbance was calculated in the exposed rock mass of landslide area based on ratings (e.g. Hoek et al., 2002; Rose et al., 2018) and its value ranges from 0 for undisturbed in situ rock masses to 1 for highly disturbed rock masses. The value of *'D'* was assigned as zero to calculate the Hoek-Brown constants (m_b, s) of rock mass.

$$m_b = m_i exp\left(\frac{GSI-100}{28-14D}\right) \quad (7)$$

$$s = exp\left(\frac{GSI-100}{9-3D}\right) \quad (8)$$

$$a = \frac{1}{2} + \frac{1}{6}\left(e^{\frac{-GSI}{15}} - e^{\frac{-20}{3}}\right) \quad (9)$$

The cross-section of landslide intersected from a head scarp to the toe and the lithological variation was reconstructed based on fundamental concepts and field survey data. The orientations of the major joint set were traced out that signify the contribution to the landslide event. Figure 8 shows details of the 2D model and cross-section which was subsequently computed in numerical analysis. Rock exposure in the modelling site consisted of phyllite, meta-sandstone, schist, and their geotechnical parameters were assigned as shown in Table 2. The groundwater conditions in jointed rock mass are inferred which lies at a few meters depth and the model was run by considering variation of water level depths.

A well-known finite element method (FEM) was chosen to model the failure mechanism of large-scale landslides in the modeling site. The model setup was created by triangulated meshes of finite-sized elements (Fig. 9). The fundamental assumption in the modeling approach has followed the displacements within an element can be accurately interpolated from the displacements of its nodal points of triangular meshes (Duncan, 1996; Liu and Quek 2014; Wang et al., 2019). After applying appropriate boundary conditions, the nodal

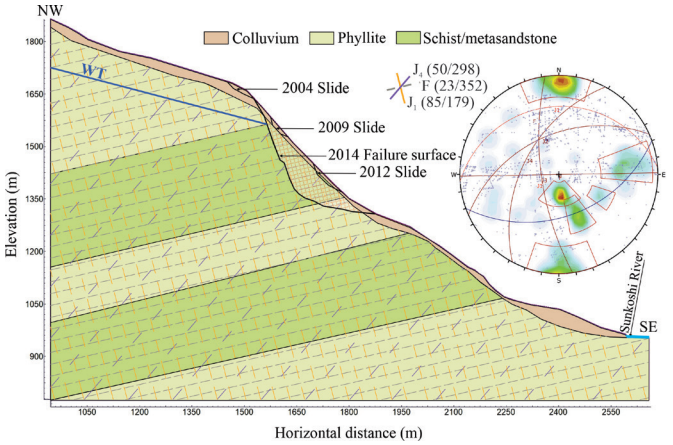

Fig. 8: 2D-Geological model showing past landslide events and discontinuities pattern.

Table 2: Rock strength parameters based on laboratory investigation and field observation.

Strength parameters	Schist/ meta-sandstone	Phyllite
Young's modulus (E), MPa	7000	6500
Poisson's ratio (ν)	0.29	0.18
Unit weight (γ), kN/m^3	28	26
Friction angle (ϕ)°	46	32
Cohesion (c), kN/m^3	200	75
Intact compressive strength (δ), MPa	50	10
Geological strength index (GSI)	55	35
Intact rock constant, m_i	12	7
m_b	2.01	0.69
s	0.0013	0.0002
a	0.51	0.52

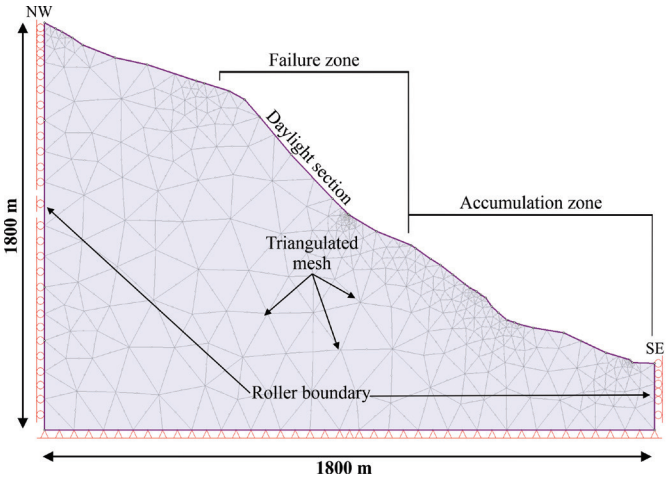

Fig. 9: 2D FEM model of slope showing six nodded triangulated mesh and roller boundary condition.

displacements were determined by using the matrix stiffness equation of Hoek-Brown criterion. The stresses and strains within each element were calculated from nodal displacements in the computing process. Linear and non-linear algorithms or functions can be simulated in FEM. The present study has adopted a non-linear equation due to the accountability of more realistic behaviours of complex deformation to assess the mechanism from initiation to failure (Singh et al., 2007; Schmid et al., 2016). Thus, the analytical domain was set up in Phase2 by creating six-nodded triangulated meshes (Fig. 9). Roller boundary conditions were implemented after adjustment of original boundaries by iteration of multiple simulations on both sides of the slope by allowing them to move freely in the vertical direction (Fu and Liao, 2010; Schmid et al., 2016).

Modelling and evaluation of failure mechanism

The first step of simulation in numerical model was to regenerate failed-slope geometry by a series of progressive evolution of hill-slopes. At the initial phase of deformation, small slides initiated just above the head crown of the landslide, representing a normal loading condition in the absence of discontinuities. Figure 10a illustrates a maximum horizontal displacement of approximately 5 cm along with stress conditions represented by a trajectory map. When comparing the model output with the field condition small slides were found during the initial phase of deformation as indicated by the satellite image (2004) of the landslide area. The stress conditions appeared to undergo changes influenced by the presence of the inter-foliated rock mass. A stress concentration was observed along the weaker boundaries and is shown in Figure 10b. The displacement along the slope varied between 5 and 10 cm and the satellite image (2009) was further confirmed by the presence of a small gully slide at the back slope of the main landslide body. Furthermore, a continuous process of stress accumulation due to topographic attribution and shearing action caused a reduction of shear strain within the slope. The simulation output showed that the stress accumulation zone is predominantly controlled by well-developed sets of discontinuities. The stress condition is visualized through contour plots of horizontal displacement (Fig. 10c) indicating horizontal displacements ranging from approximately 20 to 30 cm within the body of the landslide. Extracting the deformation history of this landslide revealed significant surface deformation during this phase evident from the presence of the landslide in the satellite image of 2012.

The ground deformation pattern was strongly influenced by the presence of well-developed joint surfaces and fluctuations of the groundwater level. Stress concentrations were prominent within the blocks of rock mass delineated by the boundary conditions of the discontinuity sets. Horizontal deformation reached >60 cm, primarily due to the reduction in shear strength resulting from pore water conditions along the discontinuity planes. The defined discontinuities anisotropy in the model significantly influenced and outburst of the rock mass in the horizontal direction as demonstrated by the displacement vector in Figure 10d. This deformation led to a peak stress condition eventually triggering a catastrophic Jure rock avalanche on 02 August 2014 clearly evident in the satellite image (Fig. 10d).

The geo-mechanical processes that lead to the initiation and propagation of failure vary depending on factors such as rock mass properties, slope, shape, and triggering events (Wang and Zhang, 1983; Gerrad, 1994; Brueckl and Parotidis, 2001; Wen and Chen, 2007; Petley, 2007; Lin et al., 2013; Hungr et al., 2014; Zerathe et al., 2014; Zhou and Cheng, 2015; Chung et al., 2018; Kuo et al., 2018). The three stages of the deformation and failure mechanism as described by Huang (1996a) and Zheng et al. (2022) are noticeable in the current modelling site. The tension cracks have occurred on the colluvium soil that connects to the open persistent joint surface. Uniform tension deformation along the joint surface (J_1) resulted in the creeping of the slope continuously. The steeper rupture joint surface was obstructed by the sub-horizontal high-grade metamorphic rock strata of schist/meta-sandstone became the locking section in the middle part of the landslide. The failure mechanism conceptualized according to Singeisen et al. (2022), displacement patterns associated with creeping and cracking progress caused the stress to accumulate gradually on the locking section (Fig. 11a). The profile's displacement pattern exhibits a bell-curve shape (Carey et al., 2019; Singeisen, et al., 2022). The displacement progressively rises beneath the head scarp reaches its peak at the central slope and then gradually decreases towards the landslide's toe.

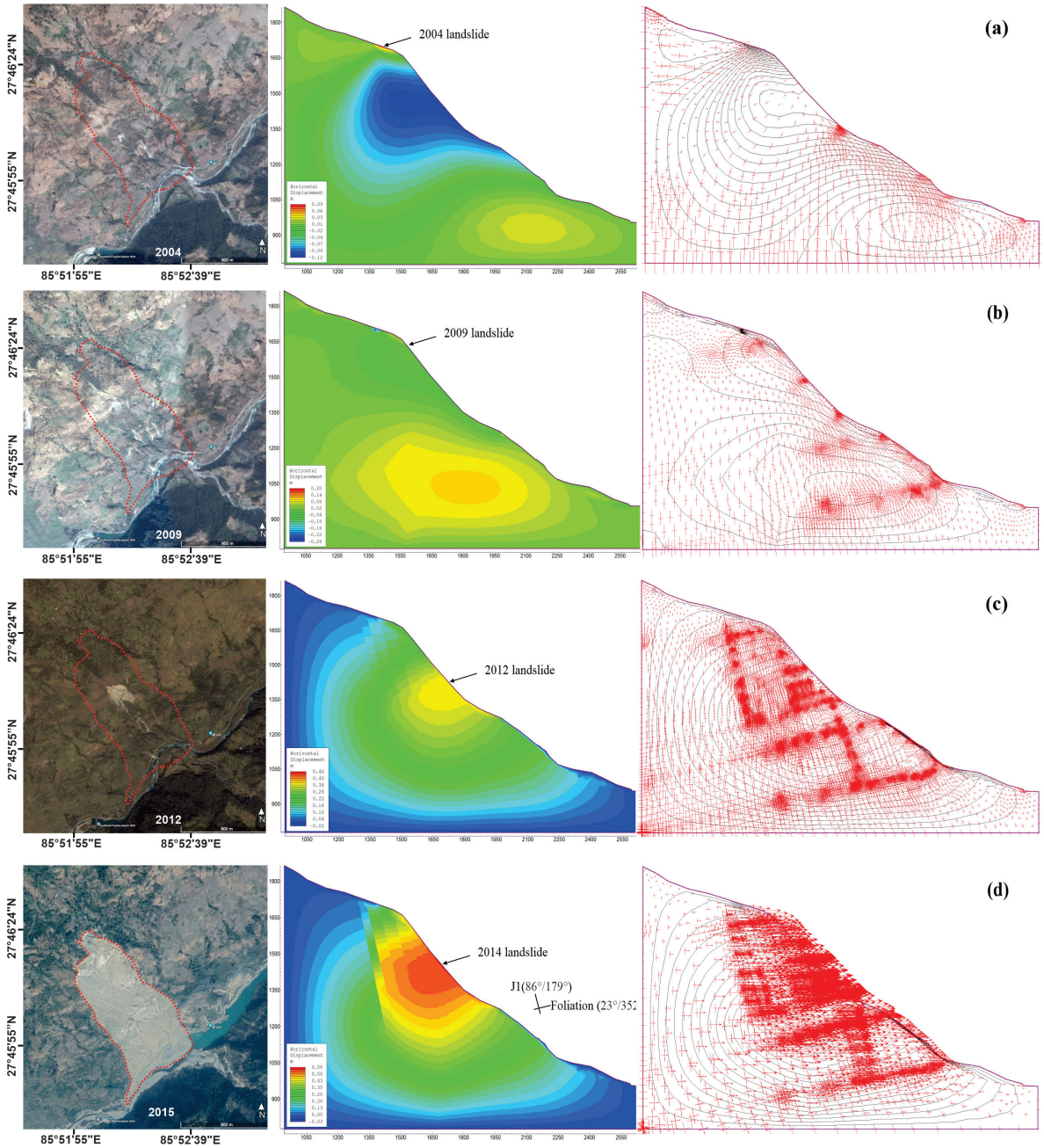

Fig. 10: Temporal failure process of landslide (a) 2004, (b) 2009, (c) 2012, (d) 2014 (catastrophic failure).

This characteristic displacement pattern resulted to internal deformation of the landslide mass (Scholtes and Donze, 2015; Wan et al., 2019).

The failure process at different deformation phases due to structural controls was found to be significantly enhanced by characteristics of discontinuities (Chung et al., 2017; Ghobadi et al., 2017). Tensile shear along the open persistent discontinuity surface and joint-step-path fracture propagation process (Scholtes and Donze, 2015; Wan et al., 2019; Singeisen et al., 2022) are found substantial for the failure. In the case of a joint-step-path failure (Fig. 11b), the failure is controlled by a network of discontinuities at the meter to centimeter scales (Singeisen et al., 2022). The failure initiated in the upper part of the slope along the slope parallel discontinuity sets and joint-step-path facture started between persistent joints by breaking the rock bridge to develop the rupture surface. The deformation in the upper slope affected the physical processes disproportionately affecting the upper slope such as initiation and expansion of tension cracks have a significant impact on slope stability (Wen and Chen, 2007; Lin et al., 2013; Hungr et al., 2014; Zerathe et al., 2014; Zhou and Cheng, 2015; Chung et al., 2018). At this stage, the displacement pattern along the profile takes on a stepped appearance. Similar to the early stage of the landslide, the initial increase in displacement magnitude occurs just below the head scarp. Displacement magnitudes remain relatively consistent in the compressional domain but they increase significantly in an exponential manner towards the rock/debris avalanche head scarp (Bozzano et al., 2011; Carey et al., 2019; Singeisen, et al., 2022).

In a rupture surface, tensile shear has occurred due to the presence of hard rock strata acting as a locking section in the middle and shared near the daylight surface. After the rainfall and groundwater flow along the rupture surface, pore water pressure is added with the residual stress on the locking section resulting in a huge rock/debris avalanche (Wang et al., 2002; Tang et al., 2014; Dhital et al., 2014; Budhathoki, 2016; Chen and Cui, 2017) (Fig. 11c). The initiation of this type of landslide is mainly controlled by the properties of the materials within which sliding occurs. Due to the concentration of topographic stresses in the middle of the slope, landslides of this type are likely to burst at the stress-accumulated zone (Korup et al., 2007; Li and Moon, 2021). This eventually resulted in the development of a huge head scarp after a rock avalanche. The displacement pattern in this failure stage is low above the head scarp just before the rock avalanche. The detached rock mass then travelled with high velocity along the slope which is not easy to measure the displacement profile (Fell et al., 2007; Glastonbury and Fell, 2008; Pfeiffer et al., 2021; Chen et al., 2021; Singeisen et al., 2022). This type of rock avalanche tends to be large and involves entire hill slopes due to the progressive accumulation of stress. The initiation can occur due to seismic forces or static changes that affect the stress state within the zone where sliding takes place (Singeisen et al., 2022).

The three-section (creep-tension-shear) failure mechanism is found to be influenced by fundamentally different rock types

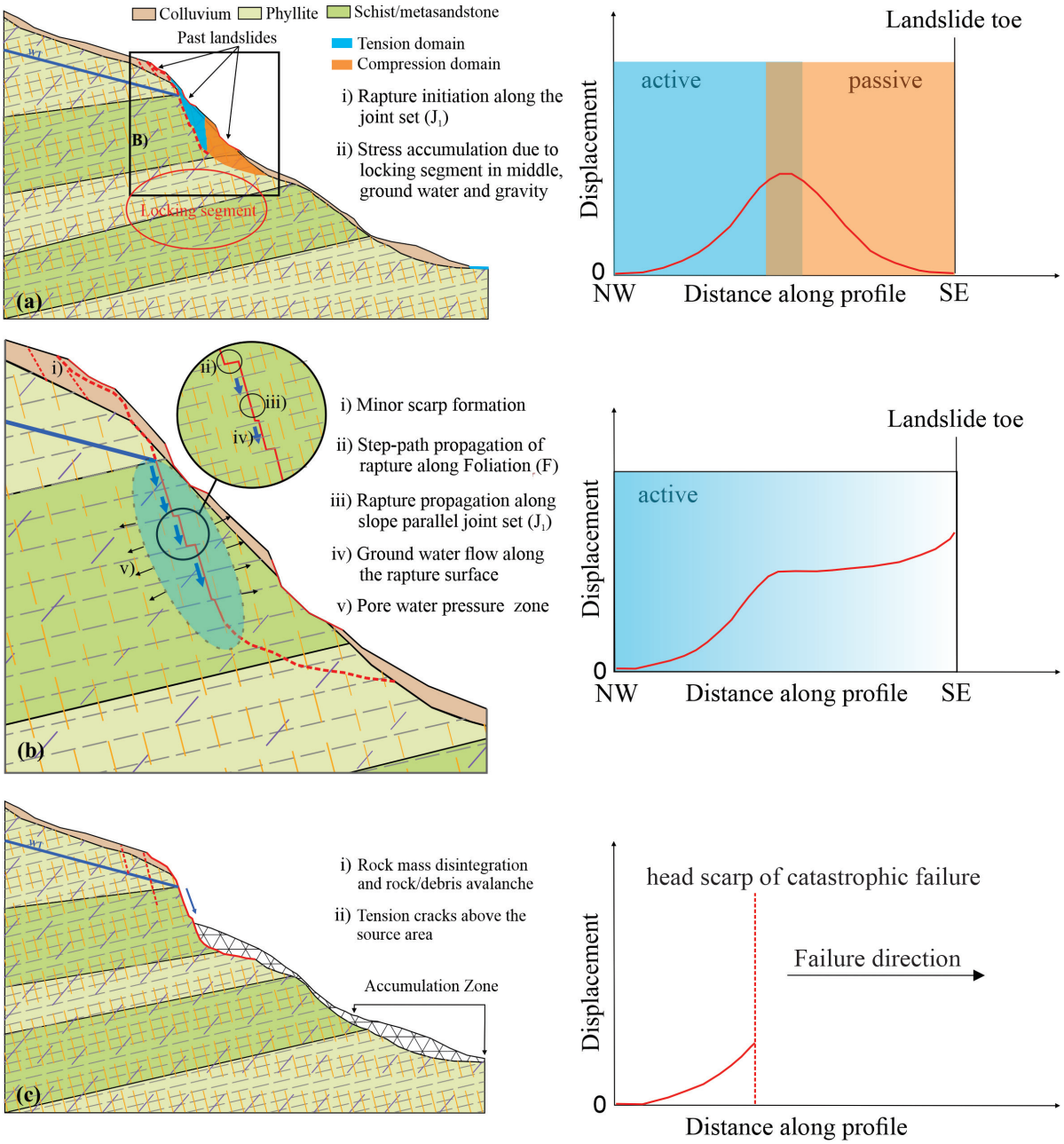

Fig. 11: Landslide failure mechanism and conceptualized displacement patterns associated with deformation stages (modified after Singeisen et al., 2022) (a) initial deformation stage, (b) uniform deformation stage, (c) accelerated deformation stage.

with differences in physico-mechanical properties of rock mass. The Paleo-Proterozoic hard rock schist associated with meta-sandstone rock slopes is fractured due to intense tectonic deformation at the western hinge of the window structure (DMG, 1980; Dhital, 2015), whereas the soft phyllite has fewer discontinuity sets and the bedding is typically consistent at larger scales. These differences in rock mass nature between the two lithology types lead to distinct structures within the rock mass that controlled the failure mechanisms of rock slopes (Stead and Wolter, 2015; Liu et al., 2020; Gerstner et al., 2023; Donati et al., 2023). Consequently, this is inherently connected to the initiation processes and occurrence of the landslides that controls the volumes, shape and size of LSLs event (Rault et al., 2019).

The genetic evolution of large-scale landslides is categorized into three deformation stages; initial, uniform, and accelerated deformation stage (Liu et al., 2018; Jeng et al., 2022). During the initial stage of deformation the slope undergoes a compressive state leading to the downward sharing of slope mass and the initiation of tension cracks (Fig. 12a). These tension cracks propagate through the underlying rock mass stratum forming rupture surfaces along persistent joint planes

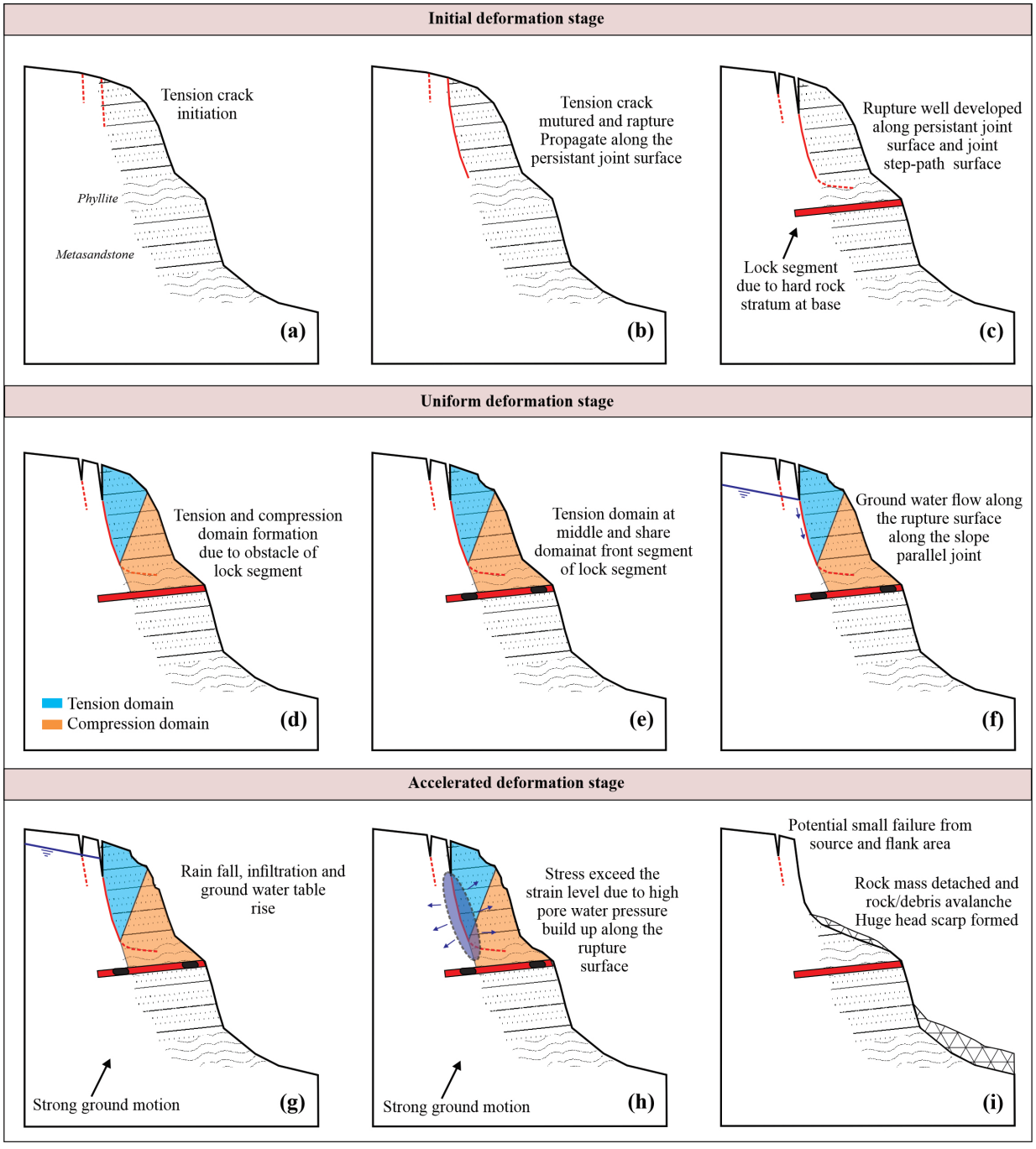

Fig. 12: Failure mechanism of large-scale landslide due to stress locking phenomenon in the modeling site of persent study based on conceptual framework of Huang (2011).

(Fig. 12b). As the deformation progresses joint step paths fracture are initiated with persistent propagation, often oriented parallel/sub-parallel to the slope gradient in the same direction. Throughout the uniform deformation stage, stress accumulation is significant resulting in the development of tension and compression domains (Fig. 12c,d). Damage to the overlying strata commences and tension shear fracturing occurs at the top (Fig. 12e). Seasonal variations in groundwater levels can cause horizontal displacement on the free face and lead to small slides (Fig. 12f). Rupture propagation stops due to the presence of hard underlying rock stratum causing the accumulation of stress at the locking segment. The rise in groundwater level (Fig. 12g) significantly increases pore water pressure along the rupture surface (Fig. 12h) ultimately resulting in a large rock debris avalanche. Large-scale landslides are triggered by abrupt alterations in stress conditions resulting from seismic activity or heavy rainfall. The detachment and accumulation processes also induced local seismic activity (Dhital et al., 2014) leading to changes in the topography and the formation of a steep head scarp at the back slope along the rupture plane (Fig. 12i).

CONCLUSION

The source area of the landslide has exhibited distinctive topographic features and unique discontinuity characteristics. It is characterized by matured joints with random shear joints parallel to obliquely oriented with the foliation and slope. Groundwater consistently flows from a weak planar surface on the southern flank, creating a steeply inclined joint plane with an orientation of 82°/065°. The weak zone extending from the southern to the northern flank, passing across the head scarp, distinguishes highly weathered soft metamorphic rock from brittle high metamorphic rock strata. Another fracture along a joint surface is observed on the northern flank, with two major sets of joints oriented at 264–298° and 335–352°. The discontinuity groups vary in persistence with low, medium, and high persistence ranging from less than 1 m to 10 m. Joint sets J_1, J_2, J_3, and J_4 have varying spacing between 0.06 m to 0.8 m. The planar joint surfaces associated with foliation exhibit rough to smooth planes with slight to moderate weathering patterns. J_3 and J_4 are obliquely oriented to the slope and show joint openings greater than 5 mm with slightly to highly weathered joint walls. The GSI of the rock mass on the sliding surface is determined to be 30–45, while on the main scarp it is estimated to be 40–65. The GSI of the rock mass on both flanks is found in the range of 25–40 due to their poor quality. The rock mass properties on the two flanks are comparable in orientation of discontinuity and GSI values.

The genetic evolution of large-scale landslides is categorized into three deformation stages: initial, uniform and accelerated deformation. During the initial stage, the slope experiences compressive forces leading to downward mass sharing and tension crack initiation. These cracks propagate through the underlying rock mass forming rupture surfaces along persistent joint planes. In the uniform deformation stage, significant stress accumulation creates tension and compression domains. Rupture propagation halts due to the presence of a hard underlying rock stratum resulting in stress accumulation at the locking segment. A rise in groundwater level resulted to increase in pore water pressure along the rupture surface that leading to larger rock debris avalanches. Large-scale landslides are triggered by abrupt changes in stress conditions caused by seismic activity or heavy rainfall. Detachment and accumulation processes may also induce local seismic activities causing alterations in the topography. The initiation and failure mechanism of LSL is controlled by the structures and associated geology of the area. This study has provided logical insights into the structural contribution of the genetic evolution of large-scale landslides and is helpful to understand the mechanism of failure in similar geo-environments.

ACKNOWLEDGEMENTS

The research study has been awarded Ph.D. support grants from the University Grants Commission (UGC), Nepal, and Grants No. PhD78/79–S&T–09. The authors are thankful to the reviewers for their valuable feedback, which significantly contributed to the improvement of manuscript.

REFERENCES

Bieniawski, Z. T., 1979, The Geomechanics classification in rock engineering application. Proceedings 4th International Congress on Rock Mechanics, v. 2, pp. 41–48.

Bieniawski, Z. T., 1989, *Engineering rock mass classification*. John Willey and Sons, New York, pp. 251.

Bossano, F., Cipriani, I., Mazzanti, P., and Prestininzi, A., 2011, Displacement patterns of a landslide affected by human activities: insights from ground-based InSAR monitoring. Natural Hazards. DOI 10.1007/s11069-011-9840-6

Broadbent, C. D. and Ko, K. C., 1971, Rheology aspects of rock slope failure. Proceeding of 13th Symposium on Rock Mechanics, Illionis, pp. 537–572.

Bruckl, E. and Parotidis, M., 2001, Estimation of large-scale mechanical properties of a large landslide on the basis of seismic results. International Journal of Rock Mechanics and Mining Sciences, v. 38, pp. 877–883.

Budhathoki, R., 2016, Cause and mechanism of 2014 Jure Rock Avalanche in Sindhupalhok District, central Nepal. MSc Thesis submitted to Tribhuvan University, Nepal (unpublished), 51+ p.

Caine, N. and Mool, P. K., 1982, Landslides in the Kolpu Khola drainage, Middle Mountains, Nepal. Mountain Research and Development, v. 2, pp. 157–173.

Carey, J. M., Massey, C. I., Lyndsell, B., and Petley, D. N., 2019, Displacement mechanisms of slow-moving landslides in response to changes in porewater pressure and dynamic stress. Earth Surface Dynamics, v. 7, pp. 707–722.

Chen, H., Li, G., Fang, R., and Zheng, M., 2021, Early Warning Indicators of Landslides Based on Deep Displacements: Applications on Jinping Landslide and Wendong Landslide, China. Frontiers in Earth Science, v. 9, pp. 1–14.

Chen, X. Z. and Cui, Y. F., 2017, The formation of the Wulipo landslide and the resulting debris flow in Dujiangyan City, China. Journal of Mountain Science, v. 14(6), pp. 1100–1112.

Chung, M., Chen, C., Lee, C., Huang, W., and Tan, C. 2018, Failure impact assessment for large-scale landslides located near human settlement: Case study in southern Taiwan. Sustainability, v. 10, pp. 1491.

Chung, M., Chen, C., Tan, C., Lee, C., and Huang, W., 2017, Investigation and assessment plan at the Xinzhuang potential large-scale landslide in southern Taiwan. World Landslide Forum, pp. 785–793.

Crosta, G. B., Imposimato, S., and Roddeman, D. G., 2003,

Numerical modelling of large landslides stability and runout. Natural Hazards and Earth System Science, v. 3(6), pp. 523–538.

Cruden, D. M. and Varnes, D. J., 1996, Landslide types and processes. In: Turner A. T., Schuster R. L. (eds.) Landslides investigation and mitigation. Transportation Research Board Special Report no. 247. National Academy Press, Washington, DC, pp. 36–75.

Cui, S., Yang, Q., Zhu, L., Pei, Z., Wang, S., and Liang, J., 2022, The role of tectonic discontinuities in triggering Large Seismic Landslides. Lithosphere. https://doi.org/10.2113/2022/3196788.

Dahal, R. K. and Hasegawa, S., 2008, Representative rainfall thresholds for landslides in the Nepal Himalaya. Geomorphology, v. 100(3–4), pp. 15.

Dahal, R. K., Hasegawa, S., Masuda, T., and Yamanaka, M., 2006, Roadside slope failures in Nepal during torrential rainfall and their mitigation. Disaster mitigation of debris flow, slope failures and landslides, v. 2, pp. 503–514.

Devkota, K. C., Regmi, A. D., Pourghasemi, H. R., Yoshida, K., Pradhan, B., Ryu, I. C., Dhital, M. R., and Althuwaynee, O. F., 2013, Landslide susceptibility mapping using certainty factor, index of entropy and logistic regression models in GIS and their comparison at Muglin-Narayanghat road section in Nepal Himalaya. Natural Hazard, v. 65, pp. 135–165.

Dhital, M. R., 2015, Geology of the Nepal Himalaya: Regional Perspective of the Classic Collided Orogen. Springer International Publishing, Switzerland. In: Lesser Himalaya of Koshi Region, pp. 163–164.

Dhital, M. R., Regmi, A. D., and Sigdel, K. P., 2014, Jure rockslide-rock avalanche and Seti glacial disaster in the Nepal Himalaya: an overview of their causes and consequences. Seventh Nepal Geological Congress (NGC-VII), Abstract Volume, Kathmandu, Nepal.

DMG, 1980, Geological map of central Nepal. Department of Mines and Geology (DMG), Kathmandu, Nepal.

Donati, D., Stead, D., and Borgatti, L., 2023, The Importance of Rock Mass Damage in the Kinematics of Landslides. Geosciences (Special Issue Landslide Behavior: From Monitoring to Kinematic Characterization through Both Traditional and Innovative Approaches), v. 13(2), 52. https://doi.org/10.3390/geosciences13020052

Duncan, J. M., 1996, State of the Art: Limit Equilibrium and Finite-Element Analysis of Slopes. Journal of Geotechnical Engineering, ASCE.

Fell, R., Glastonbury, J., and Hunter, G., 2007, Rapid landslides: the importance of understanding mechanisms and rupture surface mechanics. Quarterly Journal of Engineering Geology and Hydrogeology, v. 40(1), pp. 9–27.

Fu, W. and Liao, Y., 2010, Non-linear shear strength reduction technique in slope stability calculation. Computers and Geotechnics, v. 37(3), pp. 288–298.

Gadtaula, A. and Dhakal, S., 2019, Landslide susceptibility mapping using weight of evidence method in Haku, Rasuwa district, Nepal. Journal of Nepal Geological Society, v. 58, pp. 163–171.

Gerrard, J., 1994, The landslide hazard in the Himalayas: geological control and human action. Geomorphology, v. 10, pp. 221–230.

Gerstner, R., Fey, C., Kuschel, E.,Valentin, G., Voit, K., and Zangerl, C., 2023, Polyphase rock slope failure controlled by pre-existing geological structures and rock bridges. Bulletin of Engineering Geology and the Environment, v. 82, 363. https://doi.org/10.1007/s10064-023-03382-2

Ghobadi, M. H., Firuzi, M., and Noorzad, A., 2017, A large-scale landslide and related mechanism: a case study in the Qazvin-Rasht freeway, Iran. Environmental Earth Sciences, v. 76, pp. 478.

Glastonbury, J. and Fell, R., 2008, Geotechnical characteristics of large slow, very slow, and extremely slow landslides. Canadian Geotechnical Journal, v. 45(7), pp. 984–1005.

Hasegawa, S., Dahal, R. K., Yamanaka, M., Bhandari, N. P., Yatabe, R., and Inagaki, H., 2008, Causes of large-scale landslides in the Lesser Himalaya of central Nepal. Environmental Geology, v. 57, pp. 1423–1434.

Hoek, E. and Brown, E. T., 1997, Practical estimates of rock mass strength. International Journal of Rock Mechanics and Mining Sciences, v. 34 (8), pp. 1165–1186.

Hoek, E., 1994, Strength of rock and rock masses. ISRM News Journal, v. 2, pp. 4–16.

Hoek, E., Carranza-Torres, C., and Corkum, B., 2002, Hoek-Brown failure criterion – 2002 Edition. Proceeding NARMS_TAC Conference, Toronto, 1, pp. 267–273.

Hoek, E., Kaiser, P. K., and Bawden, W. F., 1995, Support of Underground Excavation in Hard Rock. Balkema, Rotterdam, 225 p.

Huang, R. Q. and Deng, R. G., 1993, Full simulation process for high slope substance moving. Chengdu University of Technology Press, Chengdu.

Huang, R. Q. and Li, W. L., 2008, Research on development and distribution rules of geohazards induced by Wenchuan earthquake on 12th May, 2008. Chinese Journal of Rock Mechanics and Engineering, v. 27(12), pp. 2585–2592. (In Chinese)

Huang, R. Q. and Li, W. L., 2009, Fault effect analysis of geo-hazard triggered by Wenchuan earthquake. Journal of Engineering Geology, v. 17(1), pp. 19–28. (In Chinese)

Huang, R. Q., 1996a, Studies of the geological model and formation mechanism of Xikou landslide. Proceeding of the 7th Inter Symposium on Landslides, pp. 1671–1678.

Huang, R. Q., 1996b, Full-course numerical simulation of hazardous landslides and falls. Proceeding of the 7th Inter Symposium on Landslides, pp. 1134–1140.

Huang, R. Q., Wang, S. T., and Zhang, Z. Y., 2002a, Shallow earth crust dynamics process and engineering environment research in Western China. Sichuan University Press, Chengdu.

Huang, R. Q., Zhang, Z. Y., and Wang, S. T., 1991. Systematic engineering geology studying of the stability of high slope. Chengdu University of Technology Press, Chengdu.

Huang, R., 2011, Mechanisms of large-scale landslides in China. Bulletin of Engineering Geology and the Environment, v. 71(1), pp. 161–170.

Huang, Z. Z., Tang, R. C., and Liu, S. L., 2002b, Rediscussion of the Seismogenic Structure of the Diexi Large Earthquake in 1933 and the Arc Tectonics on Jiaochang, Sichuan Province. Earthquake Research in China, v. 18 (2), pp. 183–192.

Hungr. O., leroueil, S., and Picarelli, L., 2014, The Varnes classification of landslide types, an update. Landslides. DOI: 10.1007/s10346-013-0436-y

Jeng, C. J., Chen, S. S., and Tseng, C. H., 2022, A case study on the slope displacement criterion at the critical accelerated stage triggered by rainfall and long-term creep behavior. Natural Hazards, v. 112 (6), pp. 1–36.

Korup, O., Clague, J. J., Hermanns, R. L., Hewitt, K., Strom, A. L., and Weidinger, J. T., 2007, Giant landslides, topography, and erosion. Earth and Planetary Science Letters, v. 261(3-4), pp. 578–589.

Kuo, H. L., Lin, G. W., Chen, C. W., Saito, H., Lin, C. W., Chen, H., and Chao, W. A., 2018, Evaluating critical rainfall conditions for large-scale landslides by detecting event times from seismic records. Natural Hazards and Earth System Sciences, v. 18, pp. 2877–2891.

Lei, X., Chen, X., Yang, Z., He, S., Zhu, L., and Liang, H., 2022,

A simple and robust MPM framework for modeling granular flows over complex terrains. Computers and Geotechnics, v. 149. https://doi.org/10.1016/j.compgeo.2022.104867

Li, G. K. and Moon, S., 2021, Topographic stress control on bedrock landslide size. Nature Geoscience, v. 14(5), pp. 307–313.

Lin, M., Chen, T., Lin, C., Ho, D., Cheng, K., Yin, H., and Chen, M., 2013, Detecting large-scale landslides using lidar data and aerial photos in the Namasha-Liuoguey area, Taiwan. Remote Sensing, v. 6, pp. 42–63.

Liu, G. R. and Quek, S. S., 2014, Chapter 3 - *Fundamentals for Finite Element Method*. The Finite Element Method (Second Edition). Liu, G. R. and Quek, S. S. Oxford, Butterworth-Heinemann, pp. 43–79.

Liu, H., Li, L., Li, S., and Yang, W., 2020, The Time-Dependent Failure Mechanism of Rocks and Associated Application in Slope Engineering: An Explanation Based on Numerical Investigation. Mathematical Problems in Engineering.https://doi.org/10.1155/2020/1680265

Liu, P., Huang, Z., Li, Y., Song, S., Yu, G., and Xie, M., 2018, Landsldie emergency monitoring and early warning based on situation awareness sensing. MATEC Web of Conferences, v. 175 (6): 04030. DOI:10.1051/matecconf/201817504030

Lo, K. Y. and Wai, R. S. C., 1978, Time dependent deformation of shaly rocks in southern Ontario. Canadian Geotechnical Journal, v. 15(4), pp. 537–547.

Marinos, V., Marinos, P., and Hoek, E., 2005, The geological strength index: applications and limitations. Bulletin of Engineering Geology and the Environment, v. 64(1), pp. 55–65.

Nepal, N., Chen, J., Chen, H., Wang, X., and Sharma T. P., 2019, Assessment of landslide susceptibility along the Araniko Highway in Poiqu/Bhote Koshi/Sun Koshi Watershed, Nepal Himalaya. Progress in Disaster Science, v. 3, pp. 1–10.

Nguyen, T. S., Yang, K. H., Wu, Y. K., Teng, F., Chao, W. A., and Lee, W. L., 2022, Post-failure process and kinematic behavior of two landslides: Case study and material point analysis. Computers and Geotechnics, v. 148. https://doi.org/10.1016/j.compgeo.2022.104797

Palmstrom, A., 2005, Measurement of and correlations between block size and rock quality designation (RQD). Tunnels and Underground Space Technology, v. 20, pp. 362–377.

Pathak, D., 2016, Knowledge based landslide susceptibility mapping in the Himalayas. Geoenvironmental Disasters, v. 3(1), pp. 8.

Petley, D. N., Hearn, G. J., Hart, A., Rosser, N. J., Dunning, S. A., Oven, K., and Mitchell, W. A., 2007, Trends in landslide occurrence in Nepal. Natural Hazards, v. 43, pp. 23–44.

Pfeiffer, J., Zieher, T., Schmieder, J., Rutzinger, M., and Strasser, U., 2021, Spatio-temporal assessment of the hydrological drivers of anactive deep-seated gravitational slope deformation: TheVögelsberg landslide in Tyrol (Austria). Earth Surface Process and Landforms, v. 46, pp. 1865–1881.

Phuyal, B., Thapa, P. B., and Devkota, K. C., 2022, Characterization of large-scale landslides and their susceptibility evaluation in central Nepal Himalaya. Journal of Nepal Geological Society, v. 63, pp. 109–122.

Rault, C., Robert, A., Marc, O., Hovius, N., Meunier, P., 2019, Seismic and geologic controls on spatial clustering of landslides in three large earthquakes. Earth Surface. Dynamics, v. 7(3), pp. 829–839.

Regmi, A. D., Devkota, K. C., Yoshida, K., Pradhan, B., Pourghasemi, H. R., Kumamoto, T., and Akgun, A., 2012, Application of frequency ration, statistical index, and weights-of-evidence models and their comparison in landslide susceptibility mapping in Central Nepal Himalaya. Arabian Journal of Geosciences, v. 7, pp. 725–742.

Romano, A., 2020, Physical and numerical modeling of landslide-generated tsunamis: A review. IntechOpen. doi: 10.5772/intechopen.93878

Rose, N. D., Scholz, M., Burden, J., King, M., Maggs, C., and Havaej, M., 2018, Quantifying trasitional rock mass disturbance in open pit slopes related to mining excavation. Slope stability 2018-XIV International congress on energy and mineral Resources, Asociación Nacional de Ingenieros de Minas, Seville, Spain, pp. 1273–1288.

Schimid, A., Li, A. J., Lim, K., and Nepal, K., 2016, Slope stability analysis using Phase2. Geo-China, GSP 267, pp.151–157.

Scholtes, L. and Donze, F. V., 2019, A DEM analysis of step-path failure in jointed rock slopes. Comptes Rendus Mecanique, v. 343, pp. 155–165.

Singeisen, C., Massey, C., Wolter, A., Kellett, R., Bloom, C., Stahl, T., Gasston, C., and Jones, K., 2022, Mechanism of rock slope failures triggered by the 2016 Mw 7.8 Kaikoura earthquake and implications for landslide susceptibility. Geomorphology, v. 415 (108386), pp. 1–17.

Singh, T. N.., Bhardwaj, V., Dhonta, L., and Sarkar, K., 2007, Numerical analysis of instability of slope near Rudraprayag Area, Uttaranchal, India. Jounal of Engineering Geology, v. 34(1-4), pp. 33–41.

Sonmez, H. and Ulusay, R., 1999, Modifications to the geological strength index (GSI) and their applicability to stability of slopes. International Journal of Rock Mechanics and Mining Sciences, v. 36 (6), pp. 743–760.

Stead D. and Wolter, A., 2015, A critical review of rock slope failure mechanisms: The importance of structural geology. Journal of Structural Geology, v. 74, pp. 1–23.

Stöcklin, J. and Bhattarai, K. D., 1977, Geology of Kathmandu Area and Central Mahabharat Range, Nepal Himalaya, Kathmandu: HMG/UNDP Mineral Exploration Project. Technical Report, New York (Unpublished), 86 p.

Tang, H., Zou, Z., Xiong, C., Wu, Y., Hu, X., Wang, L., Lu, S., Criss, R. E., and Li, C., 2014, An evolution model of large consequent bedding rockslides, with particular reference to the Jiweishan rockslide in Southwest China. Engineering Geology, 186, 17–27.

Thapa, P. B., 2011, Landslide susceptibility modelling in the central Nepal Lesser Himalaya. Jour. of Appl. Reg. Geol. (ZDGG), v. 162(4), pp. 405–420.

Timilsina, M., Bhandary, N. P., Dahal, R. K., and Yatabe, R., 2012, Typical morphometric and geological characteristics of largescale landslides in central Nepal. Journal of Nepal Geological Society, v. 44, pp. 45–58.

Varnes, D. J., 1978, Slope movement types and processes. In: Schuster, R. L. and Krizek, R. J. (eds.), Special Report 176: Landslides: Analysis and Control. Transportation and Road Research Board, National Academy of Science, Washington D. C., pp. 11–33.

Wan, W., Liu, J., Zhao, Y., and Fan, X., 2019, The effects of the rock bridge ligament angle and the confinement on crack coalescence in rock bridges: An experimental study and discrete element method. Comptes Rendus Mecanique, v. 347, pp. 490–503.

Wang, F. W., Sassa, K., and Wang, G., 2002, Mechanism of a long-runout landslide triggered by the August 1998 heavy rainfall in Fukushima Prefecture, Japan. Engineering Geology, v. 63, pp. 169–185.

Wang, H., Wanqing, L., and Qing-Hua, Q., 2019, Fundamental-solution-based hybrid finite element with singularity control for two-dimensional mixed-mode crack problems. Engineering Analysis with Boundary Elements, v. 108, pp. 267–278.

Wang, L. S. and Zhang, Z. Y., 1983. The basic geological mechanism model of slope rock body deformation and destruction. Collections of hydrological and engineering geology, Geological Publishing

House Press, Beijing.

Wang, S. J., 1992. The deformation mechanism and process research of Jinchuan strip mine slope. China Journal of Geotechnical Engineering, v. 14(1), pp. 1–7.

Wen, B. and Chen, H., 2007, Mineral compositions and elements concentrations as indicators for the role of groundwater in the development of landslide slip zones: a case study of large-scale landslides in the Three Gorges Area in China. Earth Science Frontiers, v. 14(6), pp. 98–106.

Wilson, A. J., Petley, D. N., and Murphy, W., 2003, Down-slope variation in geotechnical parameters and pore fluid control on a large-scale Alpine landslide. Geomorphology, v. 54, pp. 49–62.

Xu, Q., Zhang, S., and Li, W., 2011, Spatial distribution of large-scale landslides induced by the 5.12 wenchuan earthquake. Journal of Mountain Sciences, v. 8, pp. 246–260.

Zerathe, S., Lebourg, T., Braucher, R., and Bourles, D., 2014, Mid-Holocene cluster of large-scale landslides revealed in the Southwestern Alps by 36CI dating. Insight on an Alpine-scale landslide activity. Quaternary Science Reviews, v. 90, pp. 106–127.

Zhang, Z. Y. and Liu, H. C., 1990, Key engineering geology problem and research on Longyangxia Hydropower Station of Huanghe River. Chengdu University of Technology Press, Chengdu.

Zhang, Z. Y., Wang, S. T., and Wang, L. S., 1994, Principle of engineering geology analysis. Geological Publishing House Press, Beijing.

Zhao, B., Wang, Y., Luo, Y., Liang, R., Li, J., and Xie, L., 2019, Large landslides at the northeastern margin of the Bayan Har Block, Tibetan Plateau, China. Royal Society open science, v. 6(180844). DOI: 10.1098/rsos.180844

Zheng, C., He, w., Huang, C., Chen, H., and Xiao, C., 2022, Quantification of bedding rock slope deformation rate using guided wave monitoring. Frontiers in Earth Science, v. 10, pp. 1–11.

Zhou, X. P. and Cheng, H., 2015, The long-term stability analysis of 3D creeping slopes using the displacement-based rigorous limit equilibrium method. Engineering Geology, v. 195, pp. 292–300.